

## Research article

## Biomedical applications of Fe<sub>3</sub>O<sub>4</sub>-Au and Au-Fe<sub>3</sub>O<sub>4</sub> nanoparticles synthesis via a two-step pulsed laser ablation process in water

Khawla S. Khashan<sup>a,\*</sup>, Aseel A. Hadi<sup>a</sup>, Ghassan M. Sulaiman<sup>b</sup>, Asraa B. Radhi<sup>a</sup>, Mohammed H. Adu-Alghayth<sup>c</sup><sup>a</sup>Department of Applied Science, University of Technology, Sana, Baghdad, 01, 00964, Iraq<sup>b</sup>Biotechnology Division, Department of Applied Science, University of Technology, Sana, Baghdad, 01, Iraq<sup>c</sup>Department of Medical Laboratory Sciences, College of Applied Medical Sciences, University of Bisha, Saudi Arabia, Bisha, 00966, Saudi Arabia

## ARTICLE INFO

## Keywords:

Hybrid nanoparticles  
Fe<sub>3</sub>O<sub>4</sub>-Au nanocomposite  
antibacterial  
laser ablation technique  
environmentally friendly synthesis  
biocompatibility

## ABSTRACT

In this study, a two-step pulsed laser ablation (PLA) in water was used to create hybrid Fe<sub>3</sub>O<sub>4</sub>-Au nanoparticles (NPs), utilizing a fundamental Nd: YAG laser. Various characterization methods, such as Transmission Electron Microscopy (TEM), X-ray diffraction (XRD), and Fourier transform infrared spectroscopy (FTIR), were employed to analyze the properties of the hybrid NPs. FT-IR and XRD analyses successfully verified the formation of a Fe<sub>3</sub>O<sub>4</sub> NP hybrid with gold. TEM images revealed that the hybrid Fe<sub>3</sub>O<sub>4</sub>-Au colloid NPs formed semi-spherical nanostructures through aggregation. The antibacterial activities of hybrid NPs were also investigated using an agar-well diffusion assay against four pathogens: *Pseudomonas aeruginosa* (*P. aeruginosa*), *Staphylococcus aureus* (*S. aureus*), *Streptococcus mutans* (*S. mutans*), and *Acinetobacter baumannii* (*A. baumannii*). The results showed that hybrid NPs are more potent against both Gram-positive and Gram-negative strains of *Acinetobacter baumannii*, exhibiting a significant inhibition zone against the bacteria. Additionally, a hemolytic and *in vitro* toxicity assessment was performed to determine the compatibility of these NPs with human red blood cells (RBCs).

## 1. Introduction

Nanostructured materials possess remarkable mechanical, chemical, optical, electrical, and biological properties, making them highly desirable. The combination of these properties with quantum effects and a large surface area relative to their volume makes them ideal for various applications, including solar cells, antibacterial agents, photodetectors, batteries, catalysts, and others. (Khan *et al.*, 2019; Zhang *et al.*, 2017; Hamad *et al.*, 2016; Khashan *et al.*, 2017). Typically, these nanomaterials can be produced through various methods and can appear in forms such as metal oxides, composites, dots, wires, tubes, and flowers, depending on the conditions used during their preparation (Mohammed *et al.*, 2022; Farouz *et al.*, 2022; Sanad *et al.*, 2022; Dell'Aglio *et al.*, 2020; Saimon *et al.*, 2018; Khashan *et al.*, 2020).

Antibiotics are commonly used to treat infectious diseases. However, excessive use of these medications can heighten the risk of allergies in patients and lead to antimicrobial resistance. Therefore, it is becoming increasingly crucial to create new methods for effectively eliminating bacteria without contributing to antibiotic resistance. Nanostructured materials focus on localized treatment and detection, allowing for the effective separation of infectious pathogens from biological fluids through magnetic force. Research has shown that metallic and metal oxide NPs, such as titanium oxide (TiO<sub>2</sub>), zinc oxide (ZnO), and silver (Ag), exhibit antibacterial properties against various bacteria. The primary antibacterial mechanisms of these NPs include disrupting

the cell membrane, inducing oxidative stress, altering membrane permeability, and releasing toxic ions. However, the inorganic crystal structures of current NPs cannot be disassembled to regulate their release, which may lead to uncontrolled issues, such as the release of harmful substances and an increasing risk of negative impacts on the environment and living organisms.

Among these, iron oxide NPs (IONPs) have garnered significant interest due to their distinct chemical, magnetic, and electrical properties, which stem from their surface reactivity and biocompatible materials. These important attributes render them ideal for various applications, including biomedicine, environmental science, energy storage, and catalysis. Additionally, IONPs have emerged as effective antibacterial agents in comparison to traditional antibiotics (AlMalki *et al.*, 2022; Hadi *et al.*, 2021; Fadhil *et al.*, 2018; Muniz-Miranda *et al.*, 2020). Supporting innovative antimicrobial policies is vital, as the rise of antibiotic-resistant bacteria presents a significant danger to public health. IONPs, particularly those made of magnetite (Fe<sub>3</sub>O<sub>4</sub>) and maghemite (γ-Fe<sub>2</sub>O<sub>3</sub>), exhibit strong antibacterial properties due to their unique physicochemical characteristics and modes of action (Fadhil *et al.*, 2018). To enhance their effectiveness, metals such as gold (Au), palladium (Pd), silver (Ag), and platinum (Pt) are used to coat IONPs. This development has enabled the creation of multifunctional hybrid materials that combine magnetic and noble metal properties at the nanoscale. Recent techniques suggest either combining two sets of pre-existing particles or enhancing the magnetic particles through

## \*Corresponding author:

E-mail address: [khawla\\_salah@yahoo.com](mailto:khawla_salah@yahoo.com) (K.S. Khashan)

Received: 24 January, 2025 Accepted: 08 November, 2025 Epub Ahead of Print: 23 January, 2026 Published: 24 February, 2026

DOI: 10.25259/JKSUS\_154\_2025

the in-situ reduction of metal salt precursors, as the artificial methods for creating these materials are fundamentally different. In typical magnetic-metallic hybrids, clusters of metallic NP are positioned on IONPs, which range from one hundred nanometer to one micrometer in diameter and are coated with thick layers of silica or carbon. Although these hybrids are effective at their intended uses, it is still very difficult to create new synthetic processes for reliable nanomaterials (less than 100 nm in diameter) that combine magnetic and noble metal particles. Consequently, hybrid nanostructured materials, especially Fe<sub>3</sub>O<sub>4</sub>-Au NP, have recently gained prominence in medicine and optoelectronics owing to their remarkable optical and chemical properties. By incorporating additional features such as magnetic properties, gold NP can be made more biocompatible (Muniz-Miranda et al., 2020; Bakr et al., 2021; Lu et al., 2018; Caro et al., 2021). Various techniques can be employed to produce NP, such as chemical co-precipitation, thermal decomposition, hydrothermal synthesis, and laser ablation in liquid (LAL) (Khashan et al., 2017; Hasan et al., 2023; Abbas et al., 2023; Rajab et al., 2023; Mohsin et al., 2023). The latter is a relatively new method that utilizes a laser to ablate a target submerged in a solution. The pulsed LAL process is particularly innovative and versatile, allowing for the creation of various types and shapes of NP by adjusting laser parameters like energy, wavelength, and pulse duration. This technique is gaining recognition for its ability to produce high-purity NP with controlled size, composition, and shape. Pulsed laser ablation in liquid (PLAL) illustrates the principles of nanoparticle formation by showing how a high-energy laser interacts with a target in a liquid medium. Compared to traditional methods, this approach offers several advantages, including 1) ease of understanding and use, 2) the production of highly pure products without the need for additional solvents (Muniz-Miranda et al., 2020; Bakr et al., 2021), and 3) an environmentally friendly profile (Rajab et al., 2023; Mohsin et al., 2023). PLAL processes are based on several fundamental physical techniques: a) interaction between laser and material, b) plasma generation, c) nanoparticle (NP) formation, and d) effects of the liquid medium. This method offers significant advantages over traditional techniques, including simplicity, versatility, controlled production, environmental friendliness, high transparency, and superior quality of the resulting NP (Caro et al., 2021; Ghanbari et al., 2014; Xu et al., 2007; Karamipour et al., 2015; Baghayeri et al., 2018). Consequently, a two-step PLAL approach was employed to synthesize iron oxide-gold NP (IO-Au NPs), and their characterization was assessed using various methods such as FTIR, FE-SEM, UV-VIS, and Z-potential. Furthermore, the antibacterial properties against certain strains of microorganisms and biocompatibility were evaluated through hemolysis tests on human red blood cells.

## 2. Materials and Methods

A Q-switched 1064 nm Nd: YAG pulsed laser was used to ablate a high-purity iron target (99.99%) contained in three milliliters of distilled water in a glass container. The iron target was ablated with 200 mJ of laser energy over 500 pulses to generate the desired NP in suspension. The resulting suspension from the laser ablation process was subsequently utilized to produce hybrid Fe<sub>3</sub>O<sub>4</sub>-Au NP by replacing the iron target with a gold target, using the same laser setting parameters.

X-ray diffractometric analyses were conducted to investigate the crystals created by the hybrid materials and the synthesized NP. The X-ray diffraction (XRD) was performed with a diffractometer (PODWE-XRD 2700AB HAO, Yuan /China), utilizing an X-ray beam set at 40 kV and 30 mA with Cu K $\alpha$  ( $\lambda = 1.5405 \text{ \AA}$ ) radiation. Additionally, Fourier Transform Infrared Spectroscopy (FTIR) was recorded in the wavenumber range of 4000 to 500 cm<sup>-1</sup> using KBr pellets and a SPECTRUM TWO N spectrometer from Japan. A Transmission Electron Microscope (TEM) (Philips/em208s, Japan) operating at 200 kV was employed to analyze the morphological characteristics of the NP produced. Furthermore, the Energy Dispersive Spectrum (EDS) (Inspect S50 FEI, Netherlands) was used to evaluate the elemental makeup of the synthesized and hybrid NP. The zeta potential was determined via a Zeta analyzer. The antibacterial efficacy of hybrid NP was evaluated using an agar-well diffusion method against four distinct bacterial species: *Pseudomonas aeruginosa* (*P.aeruginosa*), *Streptococcus mutans* (*S.mutans*), *Acinetobacter baumannii* (*A.baumannii*), and *Staphylococcus aureus* (*S.*

*aureus*). The Mueller Hinton agar medium was utilized to grow stock cultures of the bacterial isolates overnight at 37°C, after which they were refrigerated at 4°C for future use. The aim of using Mueller-Hinton agar is to evaluate its antibacterial efficacy. The manufacturer states that to create the medium, 3.8 g of the powder was combined with 100 mL of distilled water. A continuously shaking heater was employed to dissolve the powder at an increasing temperature. Following 15 min of autoclaving at 121°C, the Mueller-Hinton agar was cooled in cold water to 47°C. The dishes were then allowed to reach room temperature for 15 min. The antibacterial effectiveness of the hybrid NP was measured by repeatedly assessing the inhibitory zone with a ruler from various angles.

The hemolytic activity of hybrid NPs was also examined. Blood samples from healthy volunteers were collected in gel and EDTA tubes, mixing 1600  $\mu\text{L}$  of normal saline with 200  $\mu\text{L}$  of separated blood. Subsequently, approximately 200  $\mu\text{L}$  of the diluted blood was combined with various concentrations of NP. The samples were then incubated for 1 hour at 37°C and centrifuged for 5 minutes at 700 rpm. Finally, the absorbance was measured at 541 nm, and the hemolysis fraction was calculated using a specific formula:

$$\text{Hemolysis}(\%) = \frac{OD_s - OD_n}{OD_p - OD_n} * 100 \quad (1)$$

Where OD<sub>s</sub> is the NPs optical density, OD<sub>n</sub> is a negative control, and OD<sub>p</sub> is a positive control. The experiment was carried out according to the regulations set forth by the Food and Drug Administration, the National Institute of Health, and the Helsinki Declaration and Regulation of 1975, which outlines ethical standards for the treatment of experimental subjects. Approval was obtained from the institutional ethical committee of the Department of Applied Sciences at the University of Technology in Baghdad, Iraq, following authorization from the hospitals in the medical city (Ref. No. 4832 ASBT 8/11/2021).

## 3. Results and Discussion

XRD measurements were employed to analyze the crystalline phase of the synthesized nanostructures. Fig. 1 displays the XRD pattern for the IONP nanomaterial, labelled as curve IONPs. For reference, the data for Fe<sub>3</sub>O<sub>4</sub> (JCPDS file No. 19-0629) (Iyengar et al., 2014) is presented underneath as pink bars. The diffraction pattern for the synthesized material (curve IONPs) reveals a prominent peak at  $2\theta = 43.2$  degrees, which corresponds to the (400) plane reflection of Fe<sub>3</sub>O<sub>4</sub> NP. In contrast, the XRD pattern for gold NP (Fig. 1, curve AuNPs) shows distinct peaks at 38.5° and 44.7°, which align with the (111) and (200) planes, respectively, matching the standard Bragg reflections of the face-centred cubic lattice of gold (JCPDS 04-0784) and confirming the crystallinity of the synthesized Au NP (Liu et al., 2017). The XRD pattern for AuNPs coated with IONPs has been presented in Fig. 1, labelled as curve IO@AuNPs. It displays peaks at  $2\theta = 35.35^\circ$  and  $43.25^\circ$ , which are associated with the (311) and (400) planes. These peaks indicate the cubic structure of Fe<sub>3</sub>O<sub>4</sub> NP (referencing JCPDS file No. 19-0629). Notably, the XRD pattern for IO@AuNPs does not reveal any diffraction peaks for gold, implying that the Fe<sub>3</sub>O<sub>4</sub> layer sufficiently covers the gold surface and is thick enough to obscure the contribution from the gold core. The XRD analysis indicates that the hybrid Au@IONPs (as shown in Fig. 1) exhibit a single phase of gold with a face-centered cubic lattice structure. The limited contribution of Fe<sub>3</sub>O<sub>4</sub> to the XRD diffraction pattern of gold-coated iron oxide can be attributed to the heavy Au atoms on the particle surface shielding the core. In the Au-shell sample, three weak peaks corresponding to the (111), (200), and (220) planes of gold can be observed at approximately 38.50°, 44.75°, and 64.56°. The lack of observable diffraction peaks for Fe can probably be attributed to the heavy atom effect of gold, resulting from the creation of gold-coated Fe<sub>3</sub>O<sub>4</sub> nanostructure. Consequently, our results indicate that gold obscures the XRD signal from the core, rendering it undetectable. These results align with previously published studies (Liu et al., 2008). The strong correlation between the diffraction peaks and the crystal planes suggests the formation of a crystalline hybrid of Au and Fe<sub>3</sub>O<sub>4</sub> NPs.

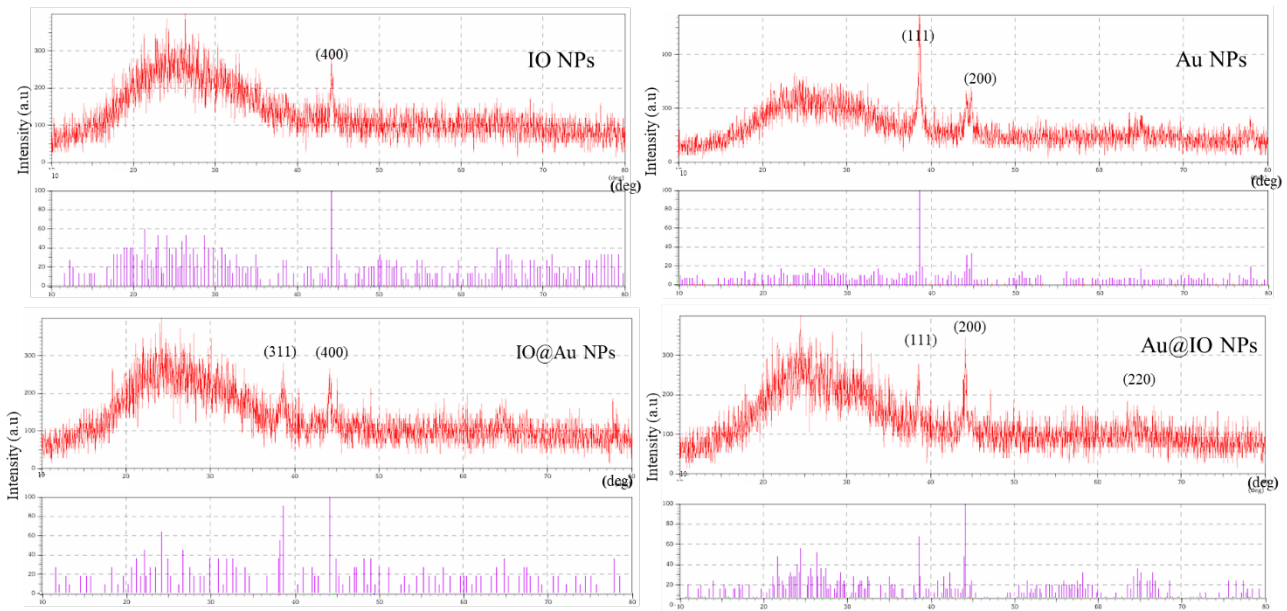


Fig. 1. XRD patterns of the stand-alone and hybrid prepared NP.

The surface chemistry of the sample was analyzed using infrared (IR) spectroscopy. The FT-IR spectra of Fe<sub>3</sub>O<sub>4</sub> NPs, Au NPs, Fe<sub>3</sub>O<sub>4</sub>@Au, and Au@Fe<sub>3</sub>O<sub>4</sub> nanocomposites exhibit similar shapes, although the intensities differ based on the concentration of the NP. The FTIR bands observed at approximately 906 cm<sup>-1</sup>, 540 cm<sup>-1</sup>, 759 cm<sup>-1</sup>, and 582 cm<sup>-1</sup> correspond to the characteristic peak of Fe-O bending vibrations (Fig. 2), which aligns with previously published studies (Tuo et al. 2015). Infrared peaks at 3326 cm<sup>-1</sup> and 1675 cm<sup>-1</sup> also show that the surface of

the produced nanocomposites has a carboxyl group. Furthermore, the band around 1635 cm<sup>-1</sup> is attributed to the bending vibration of water.

The formation of nanostructures during the LAL process is mainly due to the rapid cooling of hot plasma and its interaction with the surrounding medium. In our study, the process and chemical reaction for producing Fe<sub>3</sub>O<sub>4</sub> NP can be outlined in three steps:

(1) A single pulsed laser shot on the iron target generates high-temperature, high-pressure iron plasma at the solid-liquid interface.

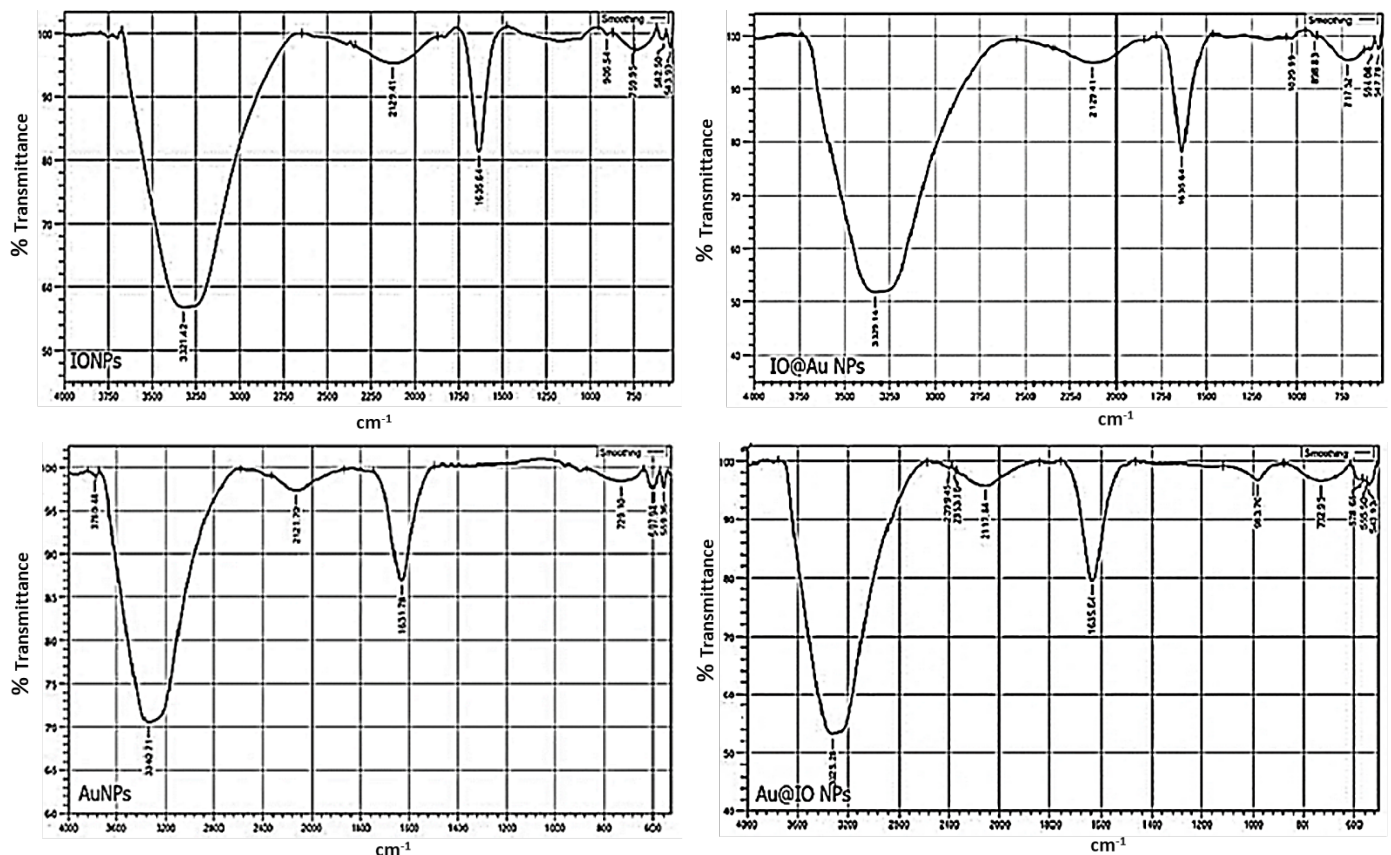
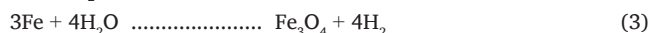


Fig. 2. FTIR spectra of prepared stand-alone Fe<sub>3</sub>O<sub>4</sub>, Au NPs, and hybrid NP.

(2) The plume area cools quickly due to the subsequent ultrasonic adiabatic expansion of the hot plasma, leading to the formation of iron clusters.

(3) Once the plasma dissipates, the created iron clusters come into contact with and interact with the solvent (water).

The LAL process can create conditions of elevated temperature and rapid cooling. Under high temperatures and pressures, the interaction of the produced Fe clusters with the solvent H<sub>2</sub>O results in the formation of Fe(OH)<sub>2</sub> NP, which subsequently decompose into FeO NP, as described by the following equations. (Abdulwahid et al., 2023; Liu et al., 2008):



In comparison to the individual Au NPs and Fe<sub>3</sub>O<sub>4</sub> NPs, the transmission spectrum of most bands diminished following the creation of Au@Fe<sub>3</sub>O<sub>4</sub> or Fe<sub>3</sub>O<sub>4</sub>@Au. This suggests that the concentration of components may have increased during the hybrid nanoparticle formation, leading to laser light scattering and a reduction in transmittance. Furthermore, the broad peaks observed around 500–700 cm<sup>-1</sup> in the spectra of Fe<sub>3</sub>O<sub>4</sub>@Au and Au@Fe<sub>3</sub>O<sub>4</sub> hybrid NP were wider than those of the individual Au NPs and Fe<sub>3</sub>O<sub>4</sub> NPs. This could be attributed to changes in the size and crystalline structure of the resulting nanocomposites. The results indicate a synergistic interface between Au NP and Fe<sub>3</sub>O<sub>4</sub> NPs, suggesting a chemical bond between the Au NPs and Fe<sub>3</sub>O<sub>4</sub> NPs (Khashan et al., 2022).

The size and shape of the individual Au NPs, Fe<sub>3</sub>O<sub>4</sub> NPs, and their hybrid Fe<sub>3</sub>O<sub>4</sub> NPs were examined using TEM. The Au NPs exhibit a nearly spherical form and are seen clustered together without distinct boundaries. The size distribution graph for the gold NPs (shown in Fig. 3a at the bottom) indicates a wide range of diameters from 4 to 40 nm, with an average size of about 21 nm. These particles tend to agglomerate (refer to Fig. 3a). Fig. 3(b) presents the TEM images and size distribution analysis (see Fig. 3b at the bottom) of the synthesized Fe<sub>3</sub>O<sub>4</sub> NPs. According to ImageJ analysis, these NPs are uniformly distributed and primarily spherical, with an average size of 81 nm and very few particles deviating from this size range (Fig. 3b). The TEM images in Fig. 3(c) illustrate the creation of core-shell Fe<sub>3</sub>O<sub>4</sub>-Au NPs in water. After applying the gold shell, the Fe<sub>3</sub>O<sub>4</sub> core appeared significantly darker compared to the previously coated magnetite NPs. The average particle size, as assessed by ImageJ, was approximately 27 nm based on TEM analysis. The obtained NPs were spherical and showed a uniform mono-dispersity in the sample, with no evidence of aggregation.

Fig. 3(d) shows the TEM image, EDX, and particle size distribution curve for Au-Fe<sub>3</sub>O<sub>4</sub> hybrid NPs. It illustrates a typical distribution of these NPs, where each Fe<sub>3</sub>O<sub>4</sub> region is covered with Au NP. The TEM image indicates no significant changes in the morphology or spherical shape of the NPs, suggesting their stability and lack of agglomeration during the reaction. Generally, the Fe<sub>3</sub>O<sub>4</sub> regions (which appear darker in the images) are about 130 nm in size, while the Au regions (which appear lighter) range from 40 to 60 nm. Additionally, the EDX elemental analysis for the points shown in Fig. 3(d) confirmed the simultaneous presence of O, Fe, and Au elements in the same locations, indicating the successful synthesis of core-shell Fe<sub>3</sub>O<sub>4</sub>-Au hybrid NPs.

To evaluate the stability of the produced samples, we measured the zeta potential after synthesis. The NPs' low positive ζ-potential suggested weak interparticle repulsion. According to theory, NPs with a ζ-potential of less than 5 mV aggregate by modulus, but NP solutions with a ζ-potential of > 30 mV have good colloidal stability (Griaznova et al., 2022). Fig. 4 displays the zeta potential values derived from each sample. All synthesized samples showed negative zeta potential, as shown by the data ζ-potential (Fig. 4). This indicates that the dispersed NPs in the suspension have negative charges and could support steric and electrostatic stabilization. The AuNPs showed a greater negative zeta potential (Fig. 4a), but compared to Fe<sub>3</sub>O<sub>4</sub> NPs, AuNPs had a greater negative charge. The Fe<sub>3</sub>O<sub>4</sub>@Au hybrid composite (Fig. 4d) demonstrated a ζ-potential magnitude with a negative charge of -11.5 mV, higher than that of Fe<sub>3</sub>O<sub>4</sub> -6.77 mV (Fig. 4b), which is a distinct

indication of Fe<sub>3</sub>O<sub>4</sub> displayed on the surface of the particles. The Au@Fe<sub>3</sub>O<sub>4</sub> hybrid composite's zeta potential value was -6.77 mV, which is lower than the Fe<sub>3</sub>O<sub>4</sub>@Au hybrid nanomaterial's zeta potential (Fig. 4c).

Fig. 5 illustrates the antibacterial effectiveness of gold (Au), Fe<sub>3</sub>O<sub>4</sub>, hybrid Fe<sub>3</sub>O<sub>4</sub>-Au, and hybrid Au-Fe<sub>3</sub>O<sub>4</sub> NPs against four different bacterial species. The agar well diffusion assay evaluated the antibacterial properties of two Gram-negative and two Gram-positive bacterial strains. In Fig. 5(a), the diameters of the inhibition zones for Au, Fe<sub>3</sub>O<sub>4</sub>, Fe<sub>3</sub>O<sub>4</sub>-Au, and Fe<sub>3</sub>O<sub>4</sub> NPs against *A. baumannii* were measured at 44, 46, 42, and 43 mm, respectively. For *P. aeruginosa*, the inhibition zone diameters for Au, Fe<sub>3</sub>O<sub>4</sub>, Fe<sub>3</sub>O<sub>4</sub>-Au, and Fe<sub>3</sub>O<sub>4</sub> NPs were 45, 43, 46, and 41 mm, as shown in Fig. 5(b). Fig. 5(c) indicates that the inhibition zones for stock Au, Fe<sub>3</sub>O<sub>4</sub>, Fe<sub>3</sub>O<sub>4</sub>-Au, and Au-Fe<sub>3</sub>O<sub>4</sub> NPs against *S. aureus* were 42, 41, 43, and 40 mm, respectively. Lastly, the inhibition zone diameters for these stocks against *S. aureus* were recorded at 40, 42, 39, and 44 mm (Fig. 5d). When compared to the control FeO<sub>4</sub> NPs, the hybrid NPs demonstrated remarkable antimicrobial efficacy against both kinds of targeted bacterial strains. Furthermore, compared to those synthesized at a lower concentration, the FeO<sub>4</sub>-Au hybrid NPs produced at a higher concentration demonstrated stronger antibacterial activity against the same bacteria. The observed increase in activity can be explained by Overton's theory of cell permeability (Tweedy, 1964), which maintains that only lipid-soluble substances can pass through the lipid bilayer surrounding the cell. Lipid solubility is vital in influencing antimicrobial activity and may explain the enhanced performance observed. Since Gram-positive bacteria possess numerous pores that facilitate the entry of foreign molecules, which can damage or kill cell membranes, as well as a thin peptidoglycan layer and teichoic acid, the NPs were more effective against these bacteria than against Gram-negative ones. Moreover, the surfaces of Gram-positive bacteria's cell walls are more negatively charged, which attracts NPs (Wang et al., 2017). NPs can fight bacteria in various ways. The ability of metal ions to damage DNA and disrupt membranes may contribute to the strong biological activity of hybrid NPs, which can denature proteins, generate reactive oxygen species (ROS) such as superoxide and peroxide, and deactivate enzymes. They have the ability to stop or restrict bacterial growth, which increases the inhibition zone (IZ) (Reda et al., 2019; Hasan et al., 2023). Antimicrobial NP therapy can either eliminate or prevent the growth of microorganisms, including protozoa, fungi, and bacteria. Treatments that kill microorganisms are referred to as microbiocidal therapies. As a result, new antimicrobial drugs could be developed and improved using these hybrid NPs. Although it has been demonstrated that NP size has a substantial impact on many applications (Varier et al., 2019), our results imply that hybrid NPs' antimicrobial efficacy is not directly correlated with their size. Rather, their toxicity seems to be more affected by variables like stability and concentration. The size of the IZ changed depending on the kind of bacteria and the concentration of NPs. Numerous industries, such as textiles, animal care, and antimicrobial packaging, can benefit from this antimicrobial. The latter uses NPs to control and prevent bacterial growth, stop liquid or gas leaks, retain moisture, and extend the shelf life of packaged foods (Lin et al., 2001). Additionally, NPs with antimicrobial properties can be used to develop antimicrobial surfaces on noncritical medical equipment. However, it is essential to consider that while exploring potential applications for antimicrobial NPs, safety regulations must be established to manage risks associated with NP ingestion, migration, inhalation, and skin absorption, all of which could pose health hazards to humans. Moreover, it is important to note that the release of NPs into the environment can lead to significant ecological issues, as they can be harmful to various organisms at elevated concentrations (Varier et al., 2019).

Utilizing NPs (NPs) and nanotechnologies as antibacterial agents offers several benefits compared to conventional antibiotics. These advantages include the capacity to simultaneously target microorganisms via multiple mechanisms, act as efficient antibiotic carriers, and circumvent current antibiotic resistance tactics like biofilm formation and bacterial membrane disruption (Reda et al., 2019). However, employing NPs as antimicrobial agents is not without its difficulties. One significant problem with current research on NPs' antibacterial mechanisms is the absence of standardized protocols. This

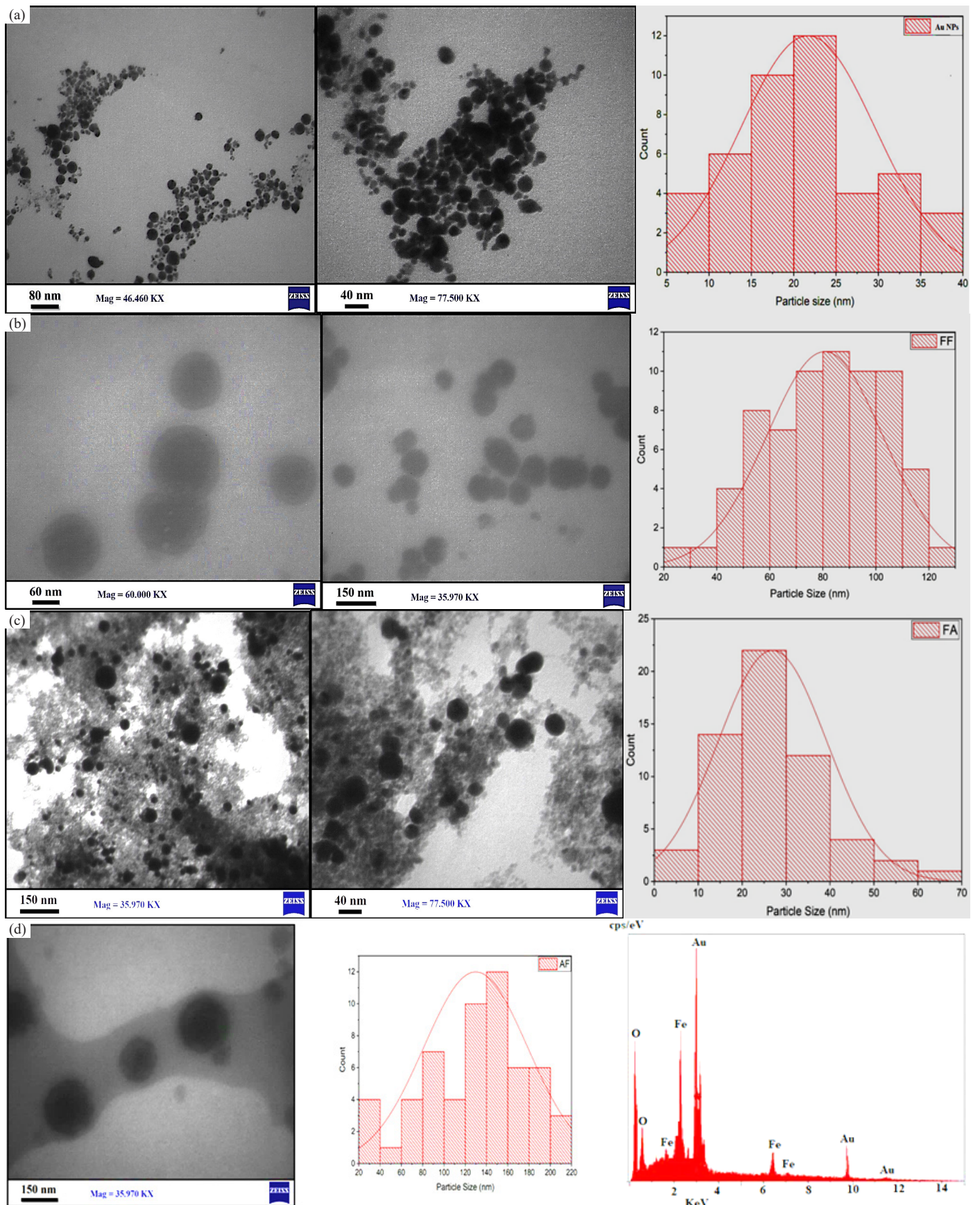
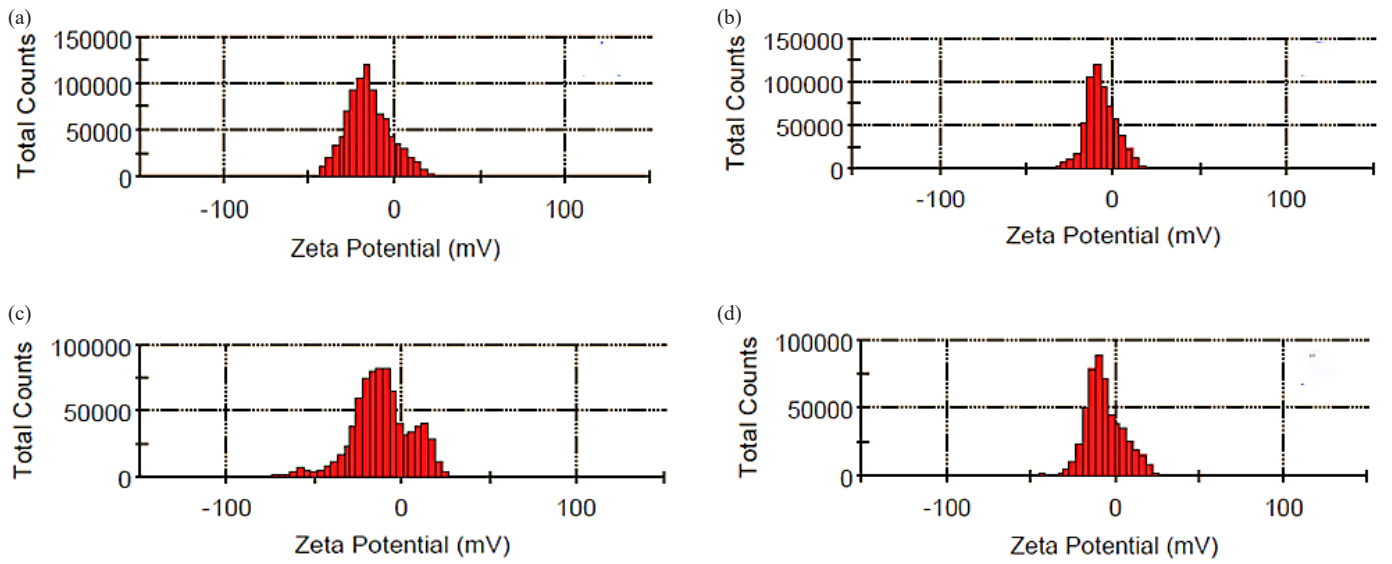
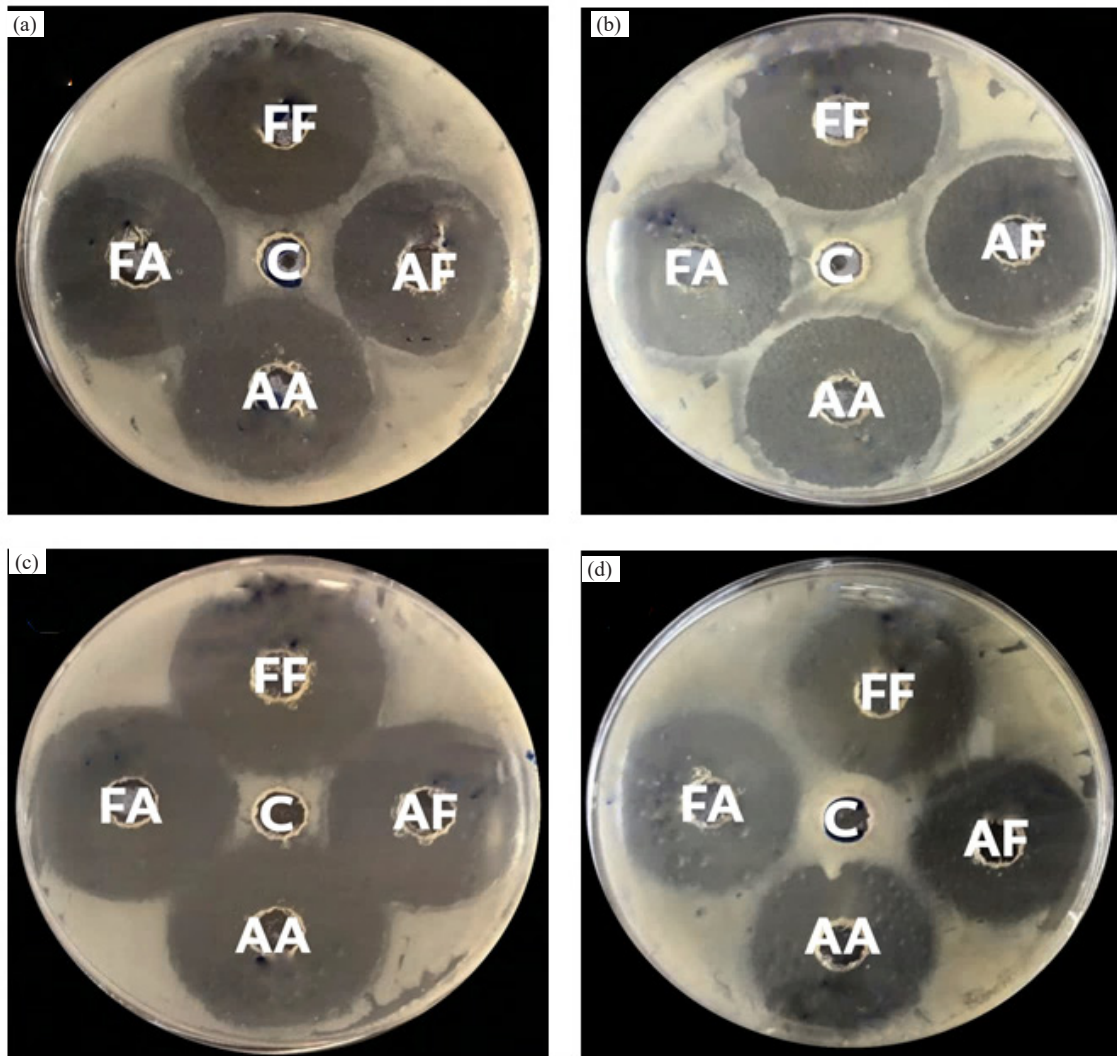


Fig. 3. TEM micrographs and size distribution of the prepared samples (a) Au NPs, (b) Fe<sub>3</sub>O<sub>4</sub> NPs, (c) Au-Fe<sub>3</sub>O<sub>4</sub> hybrid NPs, and (d) Fe<sub>3</sub>O<sub>4</sub>-Au colloid, along with size distribution right and EDX at the bottom.



**Fig. 4.** The zeta potential analysis of the synthesized NPs: (a) Au NPs prepared at 200 mJ and 500 pulses, exhibiting a zeta potential of -15 mV; (b) IONPs ( $\text{Fe}_3\text{O}_4$  NPs) synthesized under the same conditions (200 mJ, 500 pulses), with a zeta potential of -6.77 mV; (c) Au- $\text{Fe}_3\text{O}_4$  composite NPs at a composition of 49%, showing a zeta potential of -6.04 mV; and (d)  $\text{Fe}_3\text{O}_4$ -Au composite NPs containing 52% gold, displaying a zeta potential of -11.5 mV.



**Fig. 5.** The antibacterial performance of synthesis NPs Au,  $\text{Fe}_3\text{O}_4$ ,  $\text{Fe}_3\text{O}_4$ -Au, and Au- $\text{Fe}_3\text{O}_4$  NPs at stock concentrations against (a) *baumannii*, (b) *aeruginosa*, (c) *aureus*, and (d) *S. mutans*. where AA, FF, AF, and FA stand for Au that was prepared with 200 mJ for 500 pulses,  $\text{Fe}_3\text{O}_4$  was synthesized at 200 mJ for 500 pulses, hybrid Au- $\text{Fe}_3\text{O}_4$  that was produced at 59%, and  $\text{Fe}_3\text{O}_4$ -Au that was produced at 52% NPs, respectively.

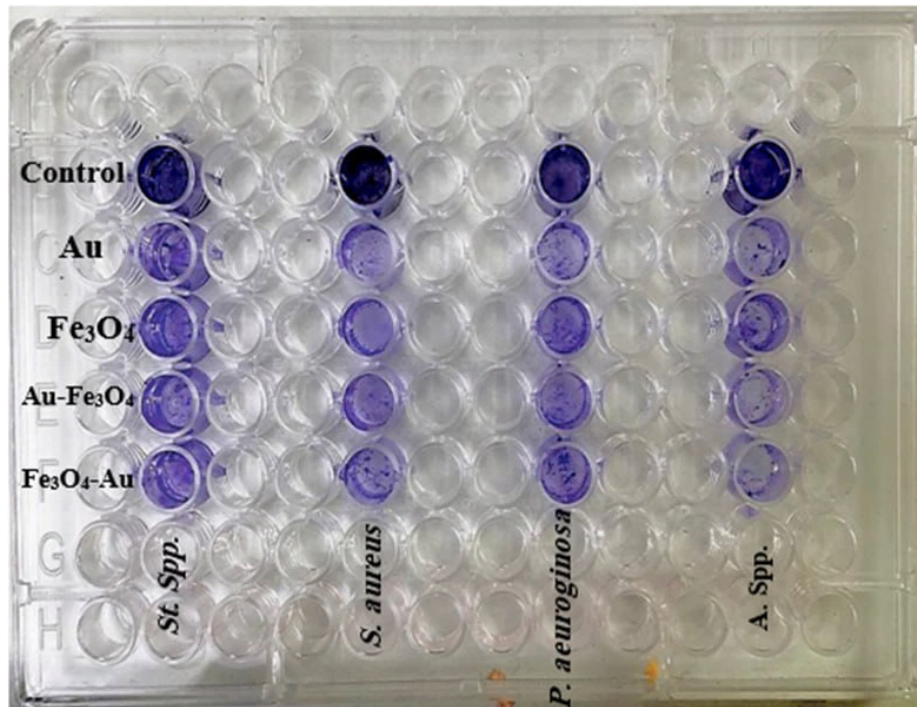


Fig. 6. The anti-biofilm activity tests of Au prepared at 200 mJ for 500 Pulses,  $\text{Fe}_3\text{O}_4$  at 200 mJ with 500 pulses, hybrid  $\text{Au-Fe}_3\text{O}_4$  at concentrations of 49%, and  $\text{Fe}_3\text{O}_4\text{-Au}$  at concentrations of 52% NPs against four bacterial species: *Streptococcus spp.*, *Staphylococcus aureus*, *Pseudomonas aeruginosa* and *Acinetobacter spp.*, and *Acinetobacter Spp.*

inconsistency makes it difficult to compare antibacterial effectiveness, as different studies focus on various strains of bacteria, NP characteristics, and exposure times. Therefore, no single technique can sufficiently illustrate the antibacterial mechanisms of all NPs because each type of NP has unique antibacterial properties. Furthermore, the use of certain types of NPs at high concentrations is limited due to their toxicity and other related concerns (Al-Omar et al., 2021; Jaber et al., 2021; Salman et al., 2023).

The crystal violet test was conducted to assess the anti-biofilm activity of gold (Au),  $\text{Fe}_3\text{O}_4$ ,  $\text{Fe}_3\text{O}_4\text{-Au}$ , and hybrid  $\text{Au-Fe}_3\text{O}_4$  NPs against 4 bacterial species, which include both gram-positive and gram-negative microorganisms: *Streptococcus Spp.*, *Staphylococcus aureus*, *Pseudomonas aeruginosa*, and *Acinetobacter Spp.* A microtiter plate assay was utilized to quantify the biofilm produced by these bacterial species (see Fig. 6). All bacterial strains demonstrated the ability to form biofilm in the biofilm formation test. After treatment with either Au NPs or  $\text{Fe}_3\text{O}_4$  NPs, there was a slight reduction of biofilm from the bottom of the well microplates; however, when Au NPs and  $\text{Fe}_3\text{O}_4$  NPs were used together, there was a significant reduction in biofilm. As shown in Fig. 6, the combination of high concentrations of Au NPs (51% and 49%) with  $\text{Fe}_3\text{O}_4$  NPs produced the most effective anti-biofilm results, leading to a notable biofilm inhibition rate across all bacterial strains (refer to Figs. 6 and 7). It was noted that the biofilm inhibition increased with higher concentrations of Au NPs, indicating a direct relationship with dose-dependent activity. All bacterial strains tested were capable of forming biofilms in different quantities, as indicated by the optical density (OD) values measured at 541 nm (see Histogram Fig. 7). The strains were classified as moderate biofilm producers (*Staphylococcus aureus*, *Acinetobacter spp.*) and strong biofilm producers (*Streptococcus Spp.*, *Pseudomonas aeruginosa*) based on their OD values, following the classification by Stepanović (Stepanović et al., 2007). The current study's findings on biofilm inhibition revealed

that complete inhibition ( $\text{OD} < 0.4$ ) was achieved for *S. aureus* and *Acinetobacter spp.* at concentrations of 51% and 49% of gold NPs, respectively (refer to Fig. 7b and d). The differences in the percentage of biofilm formation inhibition (Fig. 7) by  $\text{Au-Fe}_3\text{O}_4$  NPs and  $\text{Fe}_3\text{O}_4\text{-Au}$  NPs across the four bacterial strains may be attributed to various factors, including distinct chemical interactions that influence the anti-biofilm properties of the nanocomposites on different bacterial species and varying levels of antimicrobial activity (El-Khawaga et al., 2024). The suggested mechanism for the antimicrobial properties of the synthesized NPs (NPs) involves their initial attachment to and coating of microbial cell surfaces, which causes damage to the membrane and disrupts transport functions. It is believed that the NPs surround the outer layer of the microbial cells, leading to membrane rupture and alterations in the electrochemical gradient. Following this initial contact, the NPs enter the cell, generating ROS and causing oxidative stress that primarily affects the bacterial genome, plasmid DNA, and other vital organelles. In the final phase, the nanocomposite hinders ion exchange across bacterial membranes (El-Khawaga et al., 2024).

The hemocompatibility of the NPs is crucial to their capacity to deliver drugs into the body. Fig. 8 illustrates the hemolysis rate test results for Au NPs,  $\text{Fe}_3\text{O}_4$  NPs,  $\text{Fe}_3\text{O}_4 @\text{Au}$ , and  $\text{Au} @ \text{Fe}_3\text{O}_4$  hybrid NPs. It was clear that  $\text{Fe}_3\text{O}_4$  NPs induced a higher hemolysis rate compared to Au NPs and the hybrid NPs at elevated concentrations (1300-1600  $\mu\text{g}$ ). The impact of Au NPs on hemolysis at concentrations of 250, 500, and 750  $\mu\text{g}$  remained within acceptable limits, showing less than 2.78% hemolysis. At concentrations of 1000 and 1250  $\mu\text{g}$ , the hemolysis percentage was below 9%. According to the ASTM E2524-08 standard, NPs are considered damaging to blood cells if the hemolysis rate exceeds 5% (Choi et al., 2011). The same standard indicates that  $\text{Fe}_3\text{O}_4\text{-Au}$  and  $\text{Au-Fe}_3\text{O}_4$  hybrid nanomaterials are hemocompatible and can be safely used in the body at low concentrations.

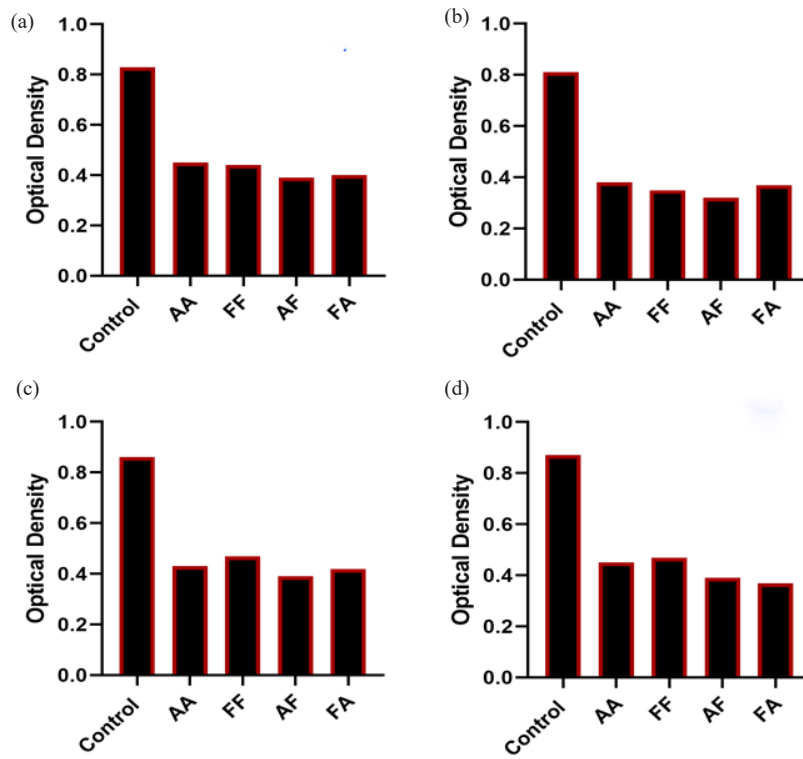


Fig. 7. Histograms of synthesized Au with 200 mJ at 500 Pulses, Fe<sub>3</sub>O<sub>4</sub> with 200 mJ for 500 pulses, hybrid Au-Fe<sub>3</sub>O<sub>4</sub> at concentrations of 49%, and Fe<sub>3</sub>O<sub>4</sub>-Au at concentrations of 52% NPs reduce biofilm formation by (a) *Streptococci Spp.*, (b) *S. aureus*, (c) *Pseudomonas aeruginosa*, and (d) *Acinetobacter Spp.*

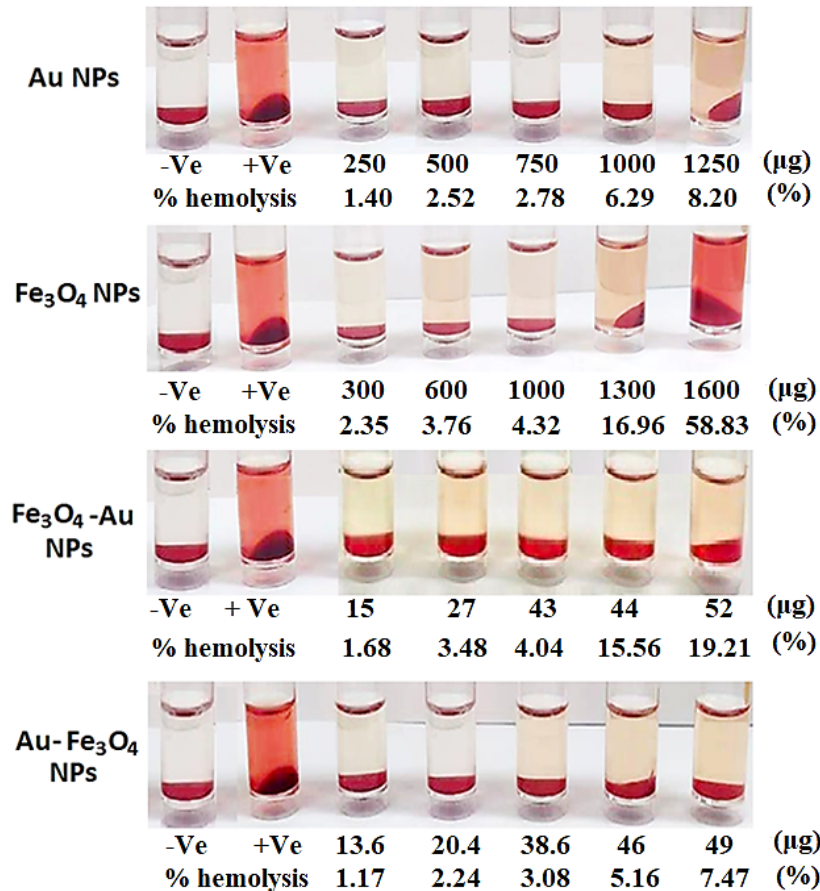


Fig. 8. Images of human red blood cells demonstrating the proportion of hemolysis upon incubation with Au, Fe<sub>3</sub>O<sub>4</sub>, Au-Fe<sub>3</sub>O<sub>4</sub>, and Fe<sub>3</sub>O<sub>4</sub>-Au NPs with varying concentrations.

#### 4. Conclusions

$\text{Fe}_3\text{O}_4/\text{Au}$  and hybrid  $\text{Fe}_3\text{O}_4/\text{Au}$  NPs were successfully produced by pulsed laser ablation (PLA) in liquid. The FTIR and XRD data verified that the hybrid NPs were successfully synthesized. TEM pictures showed a regular distribution of spherical NPs that were highly aggregated because of their magnetic properties. The hybrid NPs had a diameter of about 28 nm, whereas the average diameter of  $\text{Fe}_3\text{O}_4$  NPs was about 80 nm. The  $\text{Fe}_3\text{O}_4/\text{Au}$  hybrid suspension NPs showed antibacterial activity against both gram-positive and gram-negative bacteria, with *Acinetobacter baumannii* showing a particularly strong inhibition zone. Furthermore, as AuNP doping concentrations increased, so did the inhibition zone. The hybrid nanomaterials  $\text{Fe}_3\text{O}_4/\text{Au}$  and  $\text{Au}/\text{Fe}_3\text{O}_4$  demonstrated hemocompatibility, suggesting that they could be used in the body, albeit in small amounts.

#### CRedit authorship contribution statement

All authors contributed equally to this manuscript.

#### Declaration of competing interest

The authors declare that they have no competing financial interests or personal relationships that could have influenced the work presented in this paper.

#### Declaration of generative AI and AI-assisted technologies in the writing process

The authors confirm that there was no use of artificial intelligence (AI)-assisted technology for assisting in the writing or editing of the manuscript and no images were manipulated using AI.

#### Acknowledgment

The authors are thankful to the Deanship of Graduate Studies and Scientific Research at University of Bisha for supporting this work through the Fast-Track Research Support Program.

#### References

- Abbas, Z.A., Khashan, K.S., Hussain, Z.T., 2023. Silver-doped cadmium oxide nanoparticles synthesized by laser ablation in liquid for  $\text{NO}_2$  and  $\text{H}_2\text{S}$  gases' detection. *Plasmonics* 18, 859-869. <https://doi.org/10.1007/s11468-023-01816-x>
- Abdulwahid, F.S., Haider, A.J., Al-Musawi, S., 2023. Effect of laser parameter on  $\text{Fe}_3\text{O}_4$  NPs formation by pulsed laser ablation in liquid. *Technologies and materials for renewable energy, environment and sustainability: TMREES22Fr Metz, Grand-Est, France*, pp. 020039. <https://doi.org/10.1063/5.0129824>
- AlMalki, F.A., Khashan, K.S., Jabir, M.S., Hadi, A.A., Sulaiman, G.M., Abdulameer, F.A., Albukhaty, S., Al-Karagoly, H., Albaqami, J., 2022. Eco-friendly synthesis of carbon nanoparticles by laser ablation in water and evaluation of their antibacterial activity. *J Nanomater* 2022. <https://doi.org/10.1155/2022/7927447>
- Al-Omar, M.S., Jabir, M., Karsh, E., Kadhim, R., Sulaiman, G.M., Taqi, Z.J., Khashan, K.S., Mohammed, H.A., Khan, R.A., Mohammed, S.A.A., 2021. Gold nanoparticles and graphene oxide flakes enhance cancer cells' phagocytosis through granzyme-perforin-dependent biomechanism. *Nanomaterials* 11, 1382. <https://doi.org/10.3390/nano11061382>
- Baghayeri, M., Ansari, R., Nodehi, M., Razavianpanah, I., Veisi, H., 2018. Voltammetric aptasensor for bisphenol A based on the use of a MWCNT/ $\text{Fe}_3\text{O}_4$ @gold nanocomposite. *Mikrochim Acta* 185, 320. <https://doi.org/10.1007/s00604-018-2838-y>
- Bakr, E.A., El-Nahass, M.N., Hamada, W.M., Fayed, T.A., 2021. Facile synthesis of superparamagnetic  $\text{Fe}_3\text{O}_4$  noble metal core-shell nanoparticles by thermal decomposition and hydrothermal methods: comparative study and catalytic applications. *RSC Adv*, 11, 781-797. <https://doi.org/10.1039/D0RA08230A>
- Caro, C., Gámez, F., Quaresma, P., Páez-Muñoz, J.M., Domínguez, A., Pearson, J.R., Pernía Leal, M., Beltrán, A.M., Fernandez-Afonso, Y., De la Fuente, J.M., Franco, R., Pereira, E., García-Martín, M.L., 2021.  $\text{Fe}_3\text{O}_4$ -Au core-shell nanoparticles as a multimodal platform for *in vivo* imaging and focused photothermal therapy. *Pharmaceutics* 13, 416. <https://doi.org/10.3390/pharmaceutics13030416>
- Choi, J., Reipa, V., Hitchins, V.M., Goering, P.L., Malinauskas, R.A., 2011. Physicochemical characterization and *in vitro* hemolysis evaluation of silver nanoparticles. *Toxicol Sci* 123, 133-143. <https://doi.org/10.1093/toxsci/kfr149>

- Dell'Aglio, M., De Giacomo, A., 2020. Plasma charging effect on the nanoparticles releasing from the cavitation bubble to the solution during nanosecond pulsed laser ablation in liquid. *Appl Surf Sci* 515, 146031. <https://doi.org/10.1016/j.apsusc.2020.146031>
- El-Khawaga, A.M., Ayman, M., Hafez, O., Shalaby, R.E., 2024. Photocatalytic, antimicrobial and antibiofilm activities of  $\text{MgFe}_2\text{O}_4$  magnetic nanoparticles. *Sci Rep* 14, 12877. <https://doi.org/10.1038/s41598-024-62868-5>
- Fadhil, F.A., Hasoon, B.A., Hussein, N.N., Khashan, K.S., 2018. Preparation and characterization of CuO NPs via laser ablation under electric field and study their antibacterial activity. 4th electronic and green materials international conference 2018 (EGM 2018) Bandung, Indonesia, pp. 020002. <https://doi.org/10.1063/1.5080815>
- Farouz, M., El-Dek, S.I., ElFaham, M.M., Eldemerdash, U., 2022. Ecofriendly sustainable synthesized nano-composite for removal of heavy metals from aquatic environment. *Appl Nanosci* 12, 1585-1600. <https://doi.org/10.1007/s13204-021-02331-3>
- Ghanbari, D., Salavati-Niasari, M., Ghasemi-Kooch, M., 2014. A sonochemical method for synthesis of  $\text{Fe}_3\text{O}_4$  nanoparticles and thermal stable PVA-based magnetic nanocomposite. *Ind Eng Chem Res* 20, 3970-3974. <https://doi.org/10.1016/j.jiec.2013.12.098>
- Griaznova, O.Y., Belyaev, I.B., Sogomonyan, A.S., Zelepukin, I.V., Tikhonowski, G.V., Popov, A.A., Komlev, A.S., Nikitin, P.I., Gorin, D.A., Kabashin, A.V., Deyev, S.M., 2022. Laser synthesized core-satellite Fe-Au nanoparticles for multimodal *in vivo* imaging and *in vitro* photothermal therapy. *Pharmaceutics* 14, 994. <https://doi.org/10.3390/pharmaceutics14050994>
- Hadi, I.H., Khashan, K.S., Sulaiman, D., 2021. Cadmium sulphide (CdS) nanoparticles: Preparation and characterization. *Mater Today: Proc* 42, 3054-3056. <https://doi.org/10.1016/j.matpr.2020.12.828>
- Hamad, A., Li, L. and Liu, Z., 2016. Comparison of characteristics of selected metallic and metal oxide nanoparticles produced by picosecond laser ablation at 532 and 1064 nm wavelengths. *Applied Physics A*, 122, pp.1-15.
- Hasan, S., Khashan, K.S., Hadi, A.A., 2023. Antibacterial activity of silver nanoparticles created by one step nanosecond Nd: YAG laser ablation in water. *Adv Nat Sci: Nanosci Nanotechnol* 14, 025013. <https://doi.org/10.1088/2043-6262/acd6e6>
- Hasan, S., Khashan, K.S., Hadi, A.A., 2023. Laser-induced synthesis of palladium @ silver core-shell NPs as an effective antibacterial agent. *Plasmonics* 18, 689-699. <https://doi.org/10.1007/s11468-023-01797-x>
- Iyengar, S.J., Joy, M., Ghosh, C.K., Dey, S., Kotnala, R.K., Ghosh, S., 2014. Magnetic, X-ray and mössbauer studies on magnetite/maghemite core-shell nanostructures fabricated through an aqueous route. *RSC Adv* 4, 64919-64929. <https://doi.org/10.1039/c4ra11283k>
- Jaber, G.S., Khashan, K.S., Abbas, M.J., 2021. Study the antibacterial activity of zinc oxide nanoparticles synthesis by laser ablation in liquid. *Mater Today: Proc* 42, 2668-2673. <https://doi.org/10.1016/j.matpr.2020.12.646>
- Karamipour, S., Sadjadi, M.S., Farhadyar, N., 2015. Fabrication and spectroscopic studies of folic acid-conjugated  $\text{Fe}_3\text{O}_4/\text{Au}$  core-shell for targeted drug delivery application. *Spectrochim Acta A Mol Biomol Spectrosc* 148, 146-155. <https://doi.org/10.1016/j.saa.2015.03.078>
- Khan, I., Saeed, K., Khan, I., 2019. Nanoparticles: Properties, applications and toxicities. *Arab J Chem* 12, 908-931. <https://doi.org/10.1016/j.arabj.2017.05.011>
- Khashan, K.S. and Mahdi, F., 2017. Synthesis of ZnO: Mg nanocomposite by pulsed laser ablation in liquid. *Surface Review and Letters*, 24(07), p.1750101.
- Khashan, K.S., Taha, J.M., Abbas, S.F., 2017. Fabrication and properties of InN NPs/ Si as a photodetector. *Energy Procedia* 119, 656-661. <https://doi.org/10.1016/j.egypro.2017.07.092>
- Khashan, K.S., Sulaiman, G.M., Hussain, S.A., 2020. Synthesis and characterization of aluminum doped zinc oxide nanostructures by Nd:YAG laser in liquid. *Iraqi J Sci* 61, 2590-2598. <https://doi.org/10.24996/ijss.2020.61.10.15>
- Khashan, K.S., Hadi, A.A., Hasan, I.F., 2022. Green synthesis of  $\text{TiO}_2/\text{MWCNTs}$  composites by pulsed laser ablation in liquid. *Appl Phys A* 128. <https://doi.org/10.1007/s00339-022-05984-1>
- Lin, J., Zhou, W., Kumbhar, A., Wiemann, J., Fang, J., Carpenter, E.E., O'Connor, C.J., 2001. Gold-coated iron ( $\text{Fe}@\text{Au}$ ) nanoparticles: Synthesis, characterization, and magnetic field-induced self-assembly. *J Solid State Chem* 159, 26-31. <https://doi.org/10.1006/jssc.2001.9117>
- Liu, H.L., Sonn, C.H., Wu, J.H., Lee, K.-M., Kim, Y.K., 2008. Synthesis of streptavidin-FITC-conjugated core-shell  $\text{Fe}_3\text{O}_4$ -Au nanocrystals and their application for the purification of CD4+ lymphocytes. *Biomaterials* 29, 4003-4011. <https://doi.org/10.1016/j.biomaterials.2008.06.031>
- Liu, P., Cai, W., Zeng, H., 2008. Fabrication and size-dependent optical properties of FeO nanoparticles induced by laser ablation in a liquid medium. *J Phys Chem C* 112, 3261-3266. <https://doi.org/10.1021/jp709714a>
- Liu, Y., Kou, Q., Wang, D., Chen, L., Sun, Y., Lu, Z., Zhang, Y., Wang, Y., Yang, J., Xing, S.G., 2017. Rational synthesis and tailored optical and magnetic characteristics of  $\text{Fe}_3\text{O}_4$ -Au composite nanoparticles. *J Mater Sci* 52, 10163-10174. <https://doi.org/10.1007/s10853-017-1200-9>
- Lu, Q., Dai, X., Zhang, P., Tan, X., Zhong, Y., Yao, C., Song, M., Song, G., Zhang, Z., Peng, G., Guo, Z., Ge, Y., Zhang, K., Li, Y., 2018.  $\text{Fe}_3\text{O}_4/\text{Au}$  composite magnetic nanoparticles modified with cetuximab for targeted magneto-photothermal therapy of glioma cells. *Int J Nanomedicine* 13, 2491-2505. <https://doi.org/10.2147/IJN.S157935>
- Mohammed, S.A.A., Khashan, K.S., Jabir, M.S., Abdulameer, F.A., Sulaiman, G.M., Al-Omar, M.S., Mohammed, H.A., Hadi, A.A., Khan, R.A., 2022. Copper oxide nanoparticle-decorated carbon nanoparticle composite colloidal preparation through laser ablation for antimicrobial and antiproliferative actions against breast cancer cell line, MCF-7. *BioMed Res Int* 2022. <https://doi.org/10.1155/2022/9863616>

- Mohsin, M.H., Khashan, K.S., Sulaiman, G.M., Mohammed, H.A., Qureshi, K.A., Aspatwar, A., 2023. A novel facile synthesis of metal nitride@metal oxide (BN/Gd<sub>2</sub>O<sub>3</sub>) nanocomposite and their antibacterial and anticancer activities. *Sci Rep* 13, 22749. <https://doi.org/10.1038/s41598-023-49895-4>
- Muniz-Miranda, M., Muniz-Miranda, F., Giorgetti, E., 2020. Spectroscopic and microscopic analyses of Fe<sub>3</sub>O<sub>4</sub>/Au nanoparticles obtained by laser ablation in water. *Nanomaterials* (Basel) 10, 132. <https://doi.org/10.3390/nano10010132>
- Rajab, F.H., Taha, R.M., Hadi, A.A., Khashan, K.S., Mahdi, R.O., 2023. Laser induced hydrothermal growth of ZnO rods for UV detector application. *Opt Quant Electron* 55. <https://doi.org/10.1007/s11082-022-04473-2>
- Reda, M., Ashames, A., Edis, Z., Bloukh, S., Bhandare, R., Abu Sara, H., 2019. Green synthesis of potent antimicrobial silver nanoparticles using different plant extracts and their mixtures. *Processes* 7, 510. <https://doi.org/10.3390/pr7080510>
- Saimon, J.A., Madhat, S.N., Khashan, K.S., Hassan, A.I., 2018. Characterization of CdZnO/Si heterojunction photodiode prepared by pulsed laser deposition. *Int J Mod Phys B* 32, 1850341. <https://doi.org/10.1142/s0217979218503411>
- Salman, S., Khashan, K., Hadi, A., 2023. Green synthesis and characterization of palladium nanoparticles by pulsed laser ablation and their antibacterial activity. *Metals* 13, 273. <https://doi.org/10.3390/met13020273>
- Sanad, M.N., El-Dek, S.I., Eldemerdash, U. and ElFaham, M.M., 2022. Study of the adsorptive removal of (Fe<sup>2+</sup>) and (Ni<sup>2+</sup>) from water by synthesized magnetite/corn cobs magnetic nanocomposite. *Nano Futures*, 6(2), p.025004.
- Stepanović, S., Vuković, D., Hola, V., Di Bonaventura, G., Djukić, S., Cirković, I., Ruzicka, F., 2007. Quantification of biofilm in microtiter plates: Overview of testing conditions and practical recommendations for assessment of biofilm production by *Staphylococci*. *APMIS* 115, 891-899. [https://doi.org/10.1111/j.1600-0463.2007.apm\\_630.x](https://doi.org/10.1111/j.1600-0463.2007.apm_630.x)
- Tuo, Y., Liu, G., Dong, B., Zhou, J., Wang, A., Wang, J., Jin, R., Lv, H., Dou, Z., Huang, W., 2015. Microbial synthesis of Pd/Fe<sub>3</sub>O<sub>4</sub>, Au/Fe<sub>3</sub>O<sub>4</sub> and PdAu/Fe<sub>3</sub>O<sub>4</sub> nanocomposites for catalytic reduction of nitroaromatic compounds. *Sci Rep* 5, 13515. <https://doi.org/10.1038/srep13515>
- Tweedy, B.G., 1964. Plant extracts with metal ions as potential antimicrobial agents. *Phytopathology*, 55, 910-914. [http://doi.org/10.2529/JKSUS\\_154\\_2025](http://doi.org/10.2529/JKSUS_154_2025)
- Variar, K.M., Gudeppu, M., Chinnasamy, A., Thangarajan, S., Balasubramanian, J., Li, Y. and Gajendran, B., 2019. Nanoparticles: antimicrobial applications and its prospects. In *Advanced nanostructured materials for environmental remediation* (pp. 321-355). Springer, Cham.
- Wang, L., Hu, C., Shao, L., 2017. The antimicrobial activity of nanoparticles: Present situation and prospects for the future. *Int J Nanomedicine* 12, 1227-1249. <https://doi.org/10.2147/IJN.S121956>
- Xu, Z., Hou, Y., Sun, S., 2007. Magnetic core/shell Fe<sub>3</sub>O<sub>4</sub>/Au and Fe<sub>3</sub>O<sub>4</sub>/Au/Ag nanoparticles with tunable plasmonic properties. *J Am Chem Soc* 129, 8698-8699. <https://doi.org/10.1021/ja073057v>
- Zhang, J., Claverie, J., Chaker, M., Ma, D., 2017. Colloidal metal nanoparticles prepared by Laser ablation and their applications. *Chemphyschem* 18, 986-1006. <https://doi.org/10.1002/cphc.201601220>